ELSEVIER

NeuroImage

www.elsevier.com/locate/ynimg
NeuroImage 27 (2005) 416 – 424

Spatial specificity of cerebral blood volume-weighted fMRI responses at columnar resolution

Fuqiang Zhao, Ping Wang, Kristy Hendrich, and Seong-Gi Kim*

Department of Neurobiology, University of Pittsburgh, 3025 East Carson Street, Pittsburgh, PA 15203, USA

Received 24 December 2004; revised 10 March 2005; accepted 5 April 2005
Available online 31 May 2005

The spatial specificity of functional magnetic resonance imaging (fMRI) signals to columnar architecture remains uncertain. At columnar resolution, the specificity of intrinsic cerebral blood volume (CBV) response to orientation-selective columns in isoflurane-anesthetized cats was determined for CBV-weighted fMRI signals after injection of iron oxide at a dose of 10 mg Fe/kg. CBV-weighted fMRI data were acquired at 9.4 T with an in-plane resolution of 156 × 156 μm^2 in area 18 during visual stimulation at two orthogonal orientations. A 1-mm-thick imaging slice was selected tangential to the cortical surface. Regions with large CBV changes in response to two orthogonal orientation gratings were highly complementary. Maps of iso-orientation domains in response to these gratings were highly reproducible, suggesting that CBV-weighted fMRI has high sensitivity and specificity. The average distance between iso-orientation domains was 1.37 ± 0.28 mm (n = 10 orientations) in an anterior–posterior direction. CBV-weighted fMRI signal change in the iso-orientation domains induced by preferred orientation was 1.69 ± 0.24 (n = 10) times larger than that induced by orthogonal orientation. Our data demonstrate that CBV regulates at a submillimeter columnar scale and CBV-weighted fMRI has sufficient specificity to map columnar organization in animals.

Keywords: fMRI; Hemodynamic response; BOLD; CBV; Cortical columns; Visual cortex

Introduction

Most functional magnetic resonance imaging (fMRI) studies have been performed using conventional blood oxygenation level-dependent (BOLD) methodology (Ogawa et al., 1990) with a spatial resolution of several millimeters. For further investigation of cortical information processing, it is crucial to map submillimeter functional architecture such as cortical columns (Hubel and Wiesel, 1962). Since metabolism will occur at the site of the neuronal activity, imaging the metabolic change will yield high spatial specificity to neuronal active sites. An early oxygen consumption change, which is shown to be correlated with spiking activity in orientation-selective columns (Thompson et al., 2003), may be detected by the early negative BOLD signal (commonly referred to as the "dip") following the onset of stimulus (Malonek and Grinvald, 1996). Even though high specificity of the dip to active columnar structures has been demonstrated in well-controlled animal studies (Kim et al., 2000; Malonek and Grinvald, 1996), the utility of the BOLD dip for routine brain mapping is questionable (Buxton, 2001; Logothetis, 2000) due to poor sensitivity. Alternatively, the hemodynamic-based BOLD technique has been utilized in mapping submillimeter functional architecture (Cheng et al., 2001; Dechent and Frahm, 2000; Goodyear and Menon, 2001; Menon and Goodyear, 1999; Menon et al., 1997). However, the exact spatial extent of the stimulus-evoked hemodynamic response remains poorly understood (Duong et al., 2000; Engel et al., 1997; Hyde et al., 2001; Kim et al., 2000; Menon and Goodyear, 1999). Ultimately understanding the spatial limitation of hemodynamic responses is fundamental and critical for conducting high-resolution fMRI studies.

Since high spatial resolution can be easily achieved with intrinsic optical imaging, this technique has been prevalent in the research of spatial specificity of hemodynamic responses. With cerebral blood volume (CBV)-weighted optical imaging (570-nm wavelength), Malonek and Grinvald (1996) concluded that CBV responses are widespread and diffuse beyond the activated orientation columns within the cat visual cortex. Similarly, Erinjeri and Woolsey (2002) showed with CBV-weighted optical imaging that two mouse barrel fields cannot be easily separated during simultaneous stimulation of two neighboring whiskers. Localization of CBV responses can be improved by using data obtained only within a *few seconds* following the onset of stimulation (Sheth et al., 2004) or applying data processing approaches such as principal component analysis (Vanzetta et al., 2004). It is still not clear whether the parenchymal CBV response is specific to cortical columns. However, in tissue-specific cerebral blood flow (CBF)-based fMRI measurements (Duong et al., 2001), the CBF response is relatively specific to cat cortical columns even during a *late steady-state condition* (e.g., >10 s after stimulation onset). The difference between CBV-based intrinsic optical imaging and CBF-

* Corresponding author. Fax: +1 412 383 6799.
E-mail address: kimsg@pitt.edu (S.-G. Kim).
Available online on ScienceDirect (www.sciencedirect.com).

1053-8119/$ - see front matter © 2005 Elsevier Inc. All rights reserved.
doi:10.1016/j.neuroimage.2005.04.011

weighted fMRI measurements can be due to (i) the intrinsic difference between CBF and CBV regulation at a columnar level, and/or (ii) methodological differences between optical imaging and fMRI. To differentiate between these, CBV-weighted fMRI measurement at columnar resolution is essential. If the response of CBV-weighted fMRI is reasonably specific to cortical columns, the latter hypothesis is likely to explain the diffusiveness of CBV-weighted intrinsic optical signals.

In this report, the spatial specificity of CBV-weighted fMRI signals at columnar resolution was examined in the cat visual cortex by using monocrystalline iron oxide nanoparticles (MION) as a plasma blood volume tracer. During a steady-state condition established following the injection of MION, an increase in CBV during stimulation will induce an increase in the content of contrast agent, and consequently a decrease in MRI signal. Thus, fMRI following the injection of a contrast agent is predominantly weighted by the CBV change (Kennan et al., 1998; Mandeville et al., 1998; van Bruggen et al., 1998). CBV-weighted fMRI data were acquired at 9.4 T with a spatial resolution of 156 × 156 × 1000 μm^3 in area 18 during visual stimulation at two orthogonal orientations. The specificity and reproducibility of the CBV-weighted fMRI signal to orientation-selective columns were determined.

Materials and methods

Animal preparation and visual stimulation

Four female adolescent cats (weight: 0.79–1.56 kg, 10–15 weeks old) were studied with approval from the Institutional Animal Care and Use Committee. Cats were anesthetized with a ketamine (10–25 mg/kg) and xylazine (2.5 mg/kg) cocktail (i.m.). Each cat was orally intubated and mechanically ventilated using a pressure-driven Kent ventilator (~29–30 strokes/min) under isoflurane anesthesia (1–1.3% v/v) in a 7:3 N_2O/O_2 mixture. The femoral vein and artery were catheterized. Pancuronium bromide mixed in 5% dextrose Ringer's solution was delivered at 0.4 mg/kg/h by infusion pump. The cat was placed in a cradle and restrained in normal postural position by a head holder, consisting of ear bars and bite bar. During MRI experiments, we continuously recorded arterial blood pressure and end-tidal CO_2 (MP150, BIOPAC Systems Inc., CA). End-tidal CO_2 (Datex Omeda, Finland) was maintained in the range of 3.0–3.8%. The rectal temperature was maintained at 38.5 ± 0.5°C with a feedback hot water circulator. Arterial blood gas was measured; pCO_2 = 30.3 ± 1.3 mm Hg, pO_2 = 187.3 ± 11.4 mm Hg, and pH = 7.40 ± 0.02 mm Hg (mean ± SD, n = 4 cats). For CBV-weighted fMRI studies, a bolus of 10 mg/kg dextran-coated MION contrast agent was injected intravenously with ~1.5 ml/kg 10% dextran solution. A steady-state condition was reached within 5 min after injection and the half-life of MION in blood was found to be >6 h (data not shown).

Binocular visual stimuli were presented from a video projector (NEC, model #: MT1055; resolution 1040 × 890) onto a rear-projection screen. The screen was positioned 15 cm from the cat's eyes, covering about 37° of the visual field. Visual stimuli consisted of square-wave high-contrast moving gratings (2 cycles/s) with low spatial frequency (0.2 cycles/degree). Stimulus for a block of fMRI runs alternated between two orthogonal orientations (e.g., 0° and 90°). Since any abrupt change in the pattern of visual stimulus produces non-orientation-selective neural activity (Rao et al., 1997; Shmuel and Grinvald, 1996; Toth et al., 1996), a stationary grating pattern with the same orientation was presented during the pre- and post-stimulus periods. Three cats were studied for two orientations (0° vs. 90°), while one cat was studied for four orientations (0°, 45°, 90°, and 135°).

MRI data collection

All MRI measurements were performed on a 9.4-T magnet with a clear bore size of 31 cm, driven by a Unity INOVA console (Varian, Palo Alto, CA). The actively shielded gradient coil was either 11-cm inner diameter with a strength of 30 G/cm and a rise time of 300 μs, or 12-cm inner diameter with a strength of 40 G/cm and a rise time of 130 μs (Magnex, Oxford, UK). A 1.6-cm diameter surface coil provided radiofrequency transmission and signal reception. Multi-slice anatomic images were acquired to identify anatomical structures in the brain. The visual cortex was then positioned in the iso-center of the magnet, and magnetic field homogeneity was optimized by manual shimming. From multi-slice GE BOLD 'scout' fMRI and anatomical images, a 1-mm-thick slice tangential to the surface of the cortex containing visual area 18 was selected, mostly avoiding the surface of the cortex (see Fig. 1).

For CBV-weighted fMRI studies, T_2*-weighted images were acquired using the four-segmented gradient echo planar imaging

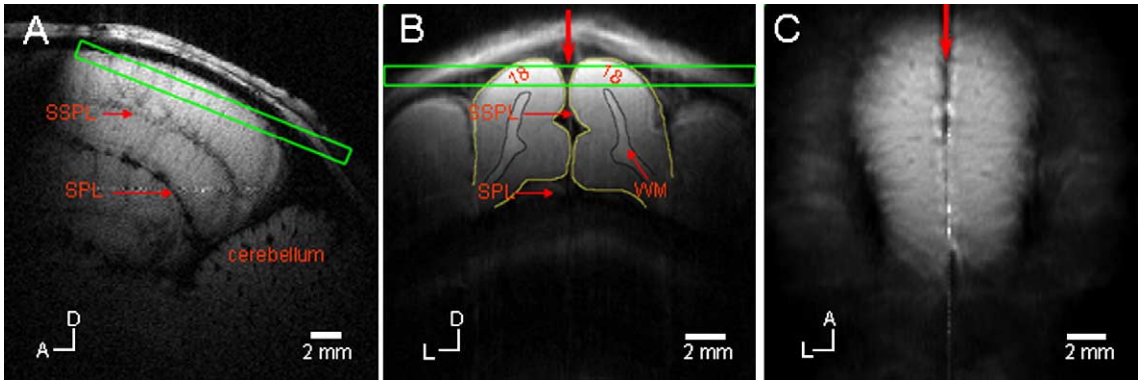

Fig. 1. Slice selection. From sagittal (A) and coronal images (B), a 1-mm-thick slice tangential to the cortex was chosen for fMRI studies (C). The fMRI imaging slice shown by the green box in A and B was positioned in area 18 at the middle of the cortex to avoid the cortical surface. Number 18, visual area 18; downward arrows (B and C), midline; SSPL, sulcus suprasplenialis; SPL, sulcus splenialis; WM, white matter. The anatomical image of B shows gray and white matter contrast, with black contours indicating boundaries between gray and white matter. A, anterior; D, dorsal; L, lateral.

(EPI) technique with a navigator echo and center-out phase-encoding scheme (Kim et al., 1996); matrix size = 128 × 128, field of view = 2 × 2 cm^2, and in-plane resolution of 156 × 156 μm^2, gradient echo time (TE) = 10 ms, and repetition time (TR) = 2 s. Flip angle of sinc-shaped RF pulse was optimized to maximize signal intensity in visual area 18. In each CBV-weighted fMRI run, ten control, ten stimulation (i.e., 20-s stimulation period), and ten control images were acquired. To increase the contrast to noise ratio, fMRI runs for each orientation were repeated 40–70 times.

Analyses of single-condition maps

Signals from all fMRI runs under the same conditions were averaged. Then, data were processed using Stimulate (Strupp, 1996) and MATLAB routines (Mathworks, MA). Statistical comparisons were made using Student's *t* test and the linear correlation method (Press et al., 1992). All data are reported as mean ± standard deviation (SD).

From data at each orientation, raw stimulation-induced subtraction maps (ΔS) were determined (without any threshold applied) as the difference between images acquired during moving vs. stationary gratings at the same orientation. To detect statistically active pixels for each single-condition, maps with a *t* value threshold $\geq$2.0 ($P < 0.05$) were then computed by comparing the image intensities acquired during the stimulation versus the control periods on a pixel-by-pixel basis. Percentage changes were calculated in statistically active pixels; images obtained during the pre-stimulus control period were considered as a baseline condition because post-stimulus fMRI signal did not return quickly to pre-stimulus signal levels. Similarly, images acquired within the initial 6 s after onset of visual stimulation were not used due to a slow hemodynamic response.

For quantitative analyses, a rectangular ROI of 26 pixels width (~4 mm) in the anterior–posterior direction and 20 pixels width (~3 mm) in the medial–lateral direction was chosen in each hemisphere. The ROIs were placed in the region of the cortex with the least curvature and with the best fMRI response. Linear correlation methods were used to determine spatial complementarities between two orthogonal orientation single-condition maps.

Analyses of differential iso-orientation maps

To determine active and inactive domains from fMRI maps in response to two orthogonal stimuli, differential maps were next obtained. Intrinsic optical imaging studies suggest that the differential signal of hemodynamic responses induced by two orthogonal stimuli correlates with spike firing rates of neurons in the active domain (Shmuel and Grinvald, 1996). For comparison with previous optical imaging studies (Frostig et al., 1990; Fukuda et al., in press), a differential iso-orientation map was obtained by subtracting percentage changes induced by one orientation stimulus (e.g., 90°) from those induced by the orthogonal orientation stimulus (e.g., 0°) for all active pixels during either orientation stimulus (Grinvald et al., 1986; Shmuel and Grinvald, 1996). Linear correlation analyses between percentage signal *changes in the differential map and single-condition maps within* the rectangular ROIs were performed (Vanzetta et al., 2004).

Resulting "patches" within the differential map were assigned to iso-orientation domains based on whether subtraction yielded positive or negative signals. An average distance between iso-orientation domains within the rectangular ROIs along the anterior–posterior direction was determined by auto-correlation analysis of the differential iso-orientation map. To estimate the functional contrast of CBV changes between "active" and "inactive" columns, averaged time courses were generated from pixels within the rectangular ROIs assigned to a selected orientation domain (e.g., 0°) during the preferred orientation stimulus (e.g., 0°) and the same pixels were used to obtain the time course during its orthogonal orientation stimulus (e.g., 90°). Then the ratio between the signal changes of a selected orientation domain stimulated by the preferred orientation to that by the orthogonal orientation was calculated.

Reproducibility test

To determine reproducibility, all fMRI data with the same stimulation paradigm were divided into two sub-groups, even and odd runs. Then, differential iso-orientation maps were determined individually from the sub-groups. Reproducibility of the differential iso-orientation domains within the rectangular ROI was determined with linear correlation analyses.

Generation of composite angle map

Four different orientations of visual stimuli were presented in the study of one animal. Preferred orientation in all active pixels during any one of four orientation stimulation was calculated on a pixel-by-pixel basis. For each orientation, signal change (ΔS) of each pixel was divided by the averaged signal change of all active pixels. This normalization process reduced signal variations due to different physiological or experimental conditions (such as a change in MION concentration due to recovery) during long measurement times. Then, a composite angle map was obtained by a pixel-by-pixel vector addition of the four iso-orientation maps with normalized ΔS as vector amplitudes and the respective stimulus orientations as vector angles (Bonhoeffer and Grinvald, 1991). As a control, a composite angle map was calculated from baseline MRI signals prior to visual stimulation. For each orientation, MRI signal intensity of each pixel was normalized by the averaged baseline signal intensity of all active pixels.

Results

CBV-weighted fMRI responses induced by two orthogonal stimuli

Five data sets in response to gratings of two orthogonal orientations (0° vs. 90° or 45° vs. 135°) were acquired from four animals. Raw stimulation-induced signal change (i.e., subtraction) maps were obtained without any statistical threshold (illustrated in Figs. 2A and B for one study of 0° vs. 90° gratings, respectively). Patchy clusters were observed in both single-condition 0° and 90° maps. More importantly, large signal changes induced by orthogonal stimuli are located within complementary territories (Figs. 2A vs. B).

Single-condition percentage change maps of 0° and 90° gratings are shown in Figs. 2C and D, respectively. It should be noted that in both percentage change maps no significant signal changes were observed at the midline with the sagittal sinus and within regions of high magnetic susceptibility (indicated by the green arrows in Fig. 2D). Peaks of percentage change maps (Figs. 2C and D) co-localize with those of corresponding raw activation

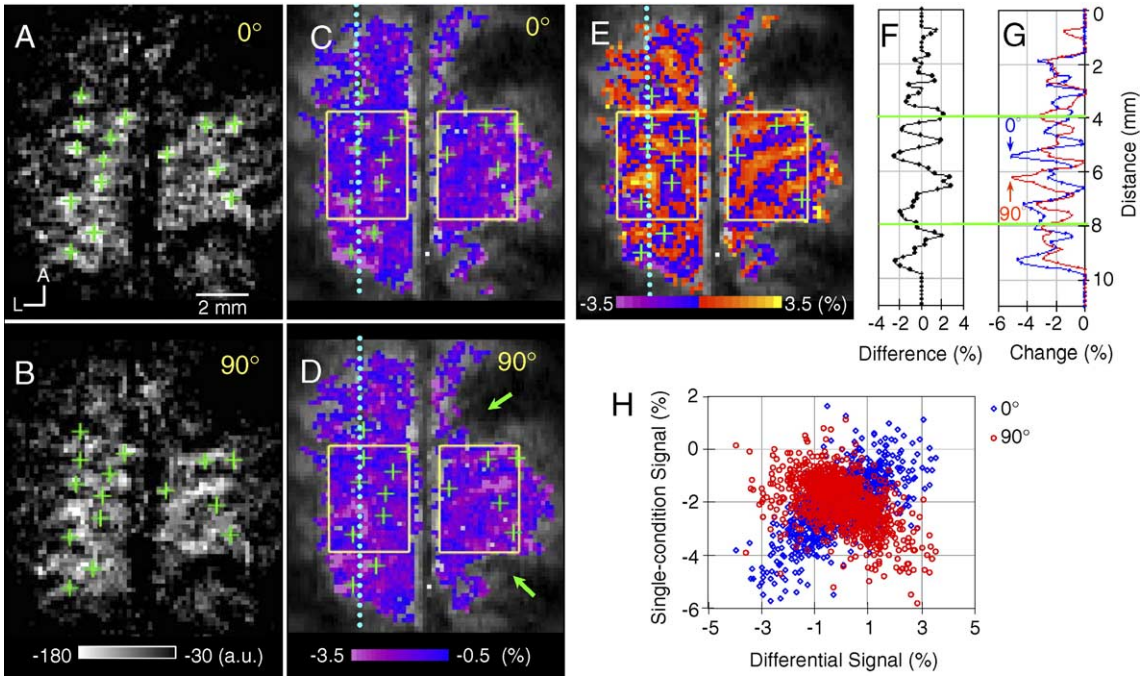

Fig. 2. Signal changes in CBV-weighted fMRI obtained from two orthogonal stimulus orientations. Raw gray-scale functional maps were determined without any threshold by subtraction of images obtained during 0° (A) or 90° (B) stimulation with those from pre-stimulus control. The bright pixels in these single-condition maps have the largest (most negative) signal changes induced by stimulation. The center of each patch on the 0° map (A) is marked with a green '+' sign; these symbols were then overlaid on all images. A, anterior; L, lateral; a.u., arbitrary unit. Single-condition percentage change maps were obtained using a t value threshold of 2.0 with moving stimuli at 0° (C) and 90° (D) orientations. Two rectangular ROIs were defined to aid in quantitative analysis and overlaid on remaining images. Green arrows in D indicate regions of high magnetic susceptibility, resulting in poor signal and consequently no detectable functional response. (E) The differential iso-orientation map was obtained by subtraction of D from C; blue/violet shows regions sensitive to 0° grating orientation, while red/yellow indicates regions with preferential response to 90° grating orientation. Patchy structures are evident. No spatial smoothing or clustering was applied. (F and G). Spatial profiles of signal changes along the dotted cyan line were obtained from the differential iso-orientation map E (black trace in F), and the single-condition percentage change maps C (blue trace in G) and D (red trace in G). Green horizontal lines in F and G indicate positions of the anterior–posterior boundaries of the ROI in maps. (H) Percentage signal changes in the 0° orientation single-condition map of C (blue diamonds) and the 90° orientation map of D (red circles) were plotted against those in the differential iso-orientation map (E) for all pixels within the rectangular ROIs; correlation coefficients are 0.58 ($P = 1.5 \times 10^{-8}$) and −0.43 ($P = 1.2 \times 10^{-4}$) for 0° and 90° single-condition maps, respectively.

maps (Figs. 2A and B). Since the two orientation domains should be complementary, a negative correlation is expected between signals induced by the two orthogonal stimuli. However, signal changes within ~3 × 4 mm^2 rectangular ROI in each hemisphere (indicated by the yellow boxes in Figs. 2C and D) have a positive correlation in four studies ($r = 0.24 \pm 0.08$, $P < 0.0005$, $n = 8$ hemispheres), no correlation in one hemisphere ($r = 0.09$, $P = 0.05$), and negative correlation in one hemisphere ($r = -0.21$, $P < 1.4 \times 10^{-6}$). This suggests that non-orientation-selective signal changes are significant.

To enable comparison with previous optical imaging studies (Frostig et al., 1990; Fukuda et al., in press), differential maps (e.g., Fig. 2E) were obtained by subtracting the single-condition percentage maps for two different orthogonal visual stimuli (e.g., Fig. 2C minus Fig. 2D). In the differential iso-orientation map (Fig. 2E), regions sensitive to 0° orientation ("0° iso-orientation domain") are shown as blue/violet, while pixels with preferential activity for the orthogonal stimulus ("90° iso-orientation domain") are red/yellow. Clearly, patchy clusters preferential to the two orthogonal stimuli are segregated. The patterns and shapes of clusters in the differential maps are consistent with those found in intrinsic optical imaging (Bonhoeffer and Grinvald, 1993). The average anterior–posterior distance between iso-orientation domains within ROIs in differential images is 1.37 ± 0.28 mm in all studies ($n = 10$ hemispheres), consistent with distances (1.0–1.4 mm) obtained by 2-deoxyglucose (Lowel et al., 1987), intrinsic optical imaging (Bonhoeffer and Grinvald, 1993), early negative BOLD signals (Kim et al., 2000), and CBF-weighted fMRI (Duong et al., 2001). This suggests that patchy structures in the differential images are orientation-selective columns.

To further examine whether orientation-selective columns can be detected by single-condition maps, two analyses were performed. First, spatial profiles of signal changes along a single line of the entire field of view in the anterior–posterior direction (indicated by dotted cyan vertical lines on the maps) were visualized (Figs. 2F and G). Negative peaks (i.e., largest signal changes) in profiles from single-condition maps (Fig. 2G) are matched relatively well with peaks of both polarities in the profile from the differential map (Fig. 2F). Second, correlation coefficients were calculated between percentage signal intensities in the differential iso-orientation map (Fig. 2E) and each of the two single condition maps (Figs. 2C and D) within the rectangular ROIs; pixel-by-pixel correspondence is shown in Fig. 2H. Since the differential iso-orientation map was calculated by subtracting percentage changes induced by 90° orientation stimulus (Fig. 2D) from those induced by 0° orientation stimulus (Fig. 2C), the 0° map has a positive correlation with the differential iso-orientation map ($r = 0.58$, $P = 1.5 \times 10^{-8}$, individual pixels shown as blue

diamonds in Fig. 2H), while the 90° map has a negative correlation ($r = -0.43$, $P = 1.2 \times 10^{-4}$, pixels shown as red circles in Fig. 2H). The average of absolute correlation values for all studies is 0.56 ± 0.11 ($n = 10$ orientations, where P values for individual studies were all $< 3.1 \times 10^{-4}$), suggesting that the single-condition maps resemble the differential iso-orientation map. Results from both spatial profile and correlation analyses indicate that high-threshold single-condition maps are able to identify columnar structures reasonably well.

Orientation selectivity of CBV-weighted fMRI signals at columnar resolution

In order to determine the selectivity of CBV-weighted fMRI to the orientation of stimuli, all pixels within both rectangular ROIs were assigned as either active or inactive domains (Fig. 3A), based on the differential image (Fig. 2E). To determine CBV-weighted fMRI signal changes induced by preferred (e.g., 0° stimulation) vs. orthogonal orientations (e.g., 90° stimulation), time courses within iso-orientation domain pixels (e.g., either red or blue pixels in Fig. 3A) were obtained during each of the two orthogonal stimuli (Fig. 3B for individual domains in one study and Fig. 3C for averaged data from all studies). The average ratio in all studies of CBV changes based on differential iso-orientation domains induced by preferred orientation vs. orthogonal orientation gratings is 1.69 ± 0.24 ($n = 10$), range between 1.54 and 2.34. Similar ratios for each of the domains in the single study of Fig. 3B are 1.60 (0° domain) and 1.58 (90° domain).

Reproducibility of differential iso-orientation maps

Despite the high signal specificity to parenchyma and the high sensitivity of CBV-weighted fMRI, reproducibility is still a concern. Fig. 4 shows the reproducibility of differential iso-orientation maps from two animals. In both differential iso-orientation maps corresponding to even (A and D) and odd (B and E) subsets of fMRI runs, dark patches indicated by green plus signs are regions selectively responding to 0° gratings. An averaged cross correlation coefficient between the two differential maps within the ROI for all studies is 0.58 ± 0.15 ($n = 10$ hemispheres, where P values for individual studies were all $<5.9 \times 10^{-5}$). This demonstrates that differential iso-orientation maps obtained by CBV-weighted fMRI are highly reproducible.

Composite angle map for four stimulus orientations

Four different grating orientations (0°, 45°, 90°, 135°) were presented in the study of one animal, enabling a composite angle map to be generated through pixel-by-pixel vector addition of the four single-condition maps (Fig. 5B). Since random noise can also generate column-like structures (Rojer and Schwartz, 1990), pre-stimulus baseline data were used as a control (Fig. 5A). Clearly, there is a major difference between the two composite maps, suggesting that the patchy iso-orientation domains observed in Fig. 5B are not due to data processing artifacts. It should be noted that no spatial smoothing was applied in Figs. 5A and B. Since the entire slice is not parallel to the surface of the cortex, only a portion of the vector summation map has properties typical of orientation columns. In the left hemisphere, changes between pixels preferentially activated by a particular stimulus orientation are smooth. For better visualization, a composite map was obtained after a 3 × 3 Gaussian filter was applied to raw data. Then, the middle of the left hemisphere shown as a white box was expanded in Fig. 5C. Even though our composite map appears to be similar to previous optical imaging data (Bonhoeffer and Grinvald, 1991; Kim and Bonhoeffer, 1994), fMRI-based "iso-orientation columns" would require further validation by comparison with multi-unit recording and/or intrinsic optical imaging data.

Discussion

Our major finding is that the CBV response is relatively specific to cat cortical columns during a *steady-state condition* (e.g., >10 s after stimulation onset), and that orientation-selective cortical columns are detectable by CBV-weighted fMRI and are even visible in simple subtraction maps of a single-condition (see Fig. 2). The orientation-selective response is ~70% higher than that of non-orientation selective response in active orientation columns for CBV-weighted fMRI. This is much higher than for CBV-weighted 570-nm wavelength intrinsic optical imaging studies, where values of ~1–5% were obtained (Frostig et al., 1990; Fukuda et al., in press). The large difference between CBV-weighted fMRI and optical imaging data may be explained by different signal sources. CBV-weighted fMRI and optical imaging differ in that CBV-weighted fMRI is sensitive to changes in plasma volume, while

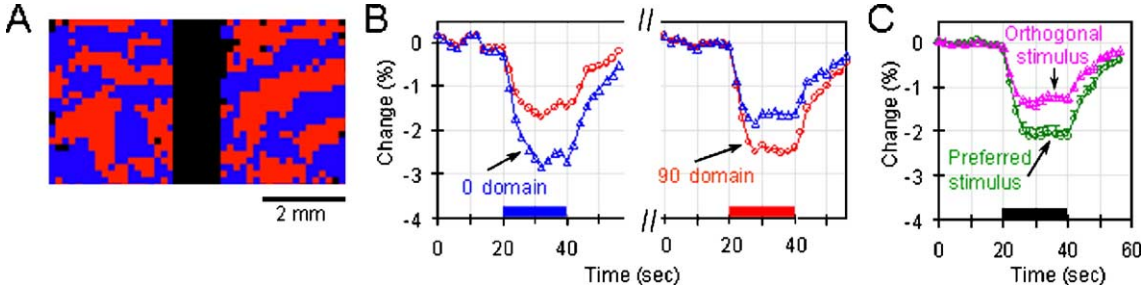

Fig. 3. Orientation selectivity of CBV-weighted fMRI signals. (A) Active pixels within both 3 × 4 mm^2 ROIs from the differential iso-orientation map shown in Fig. 2E are assigned to either 0° (blue) or 90° (red) domain. (B) Time courses of 0° and 90° iso-orientation domains from the single study in A in response to 0° and 90° grating orientations; the blue traces are the time course of the 0° iso-orientation domain (blue pixels in A) during 0° (left panel) and 90° stimulation (right panel); similarly, the red traces are the time course of the 90° iso-orientation domain (red pixels in A) during 90° (right panel) and 0° stimulation (left panel). (C) Averaged time courses from all data sets (both hemispheres) for all studies ($n = 10$) with two orthogonal stimuli were obtained from iso-orientation domains in response to stimulation with preferred (green trace) and orthogonal (pink trace) orientations. A bar under the time courses indicates the 20-s visual stimulation period (B and C). For clarity, only one side of SEM is shown.

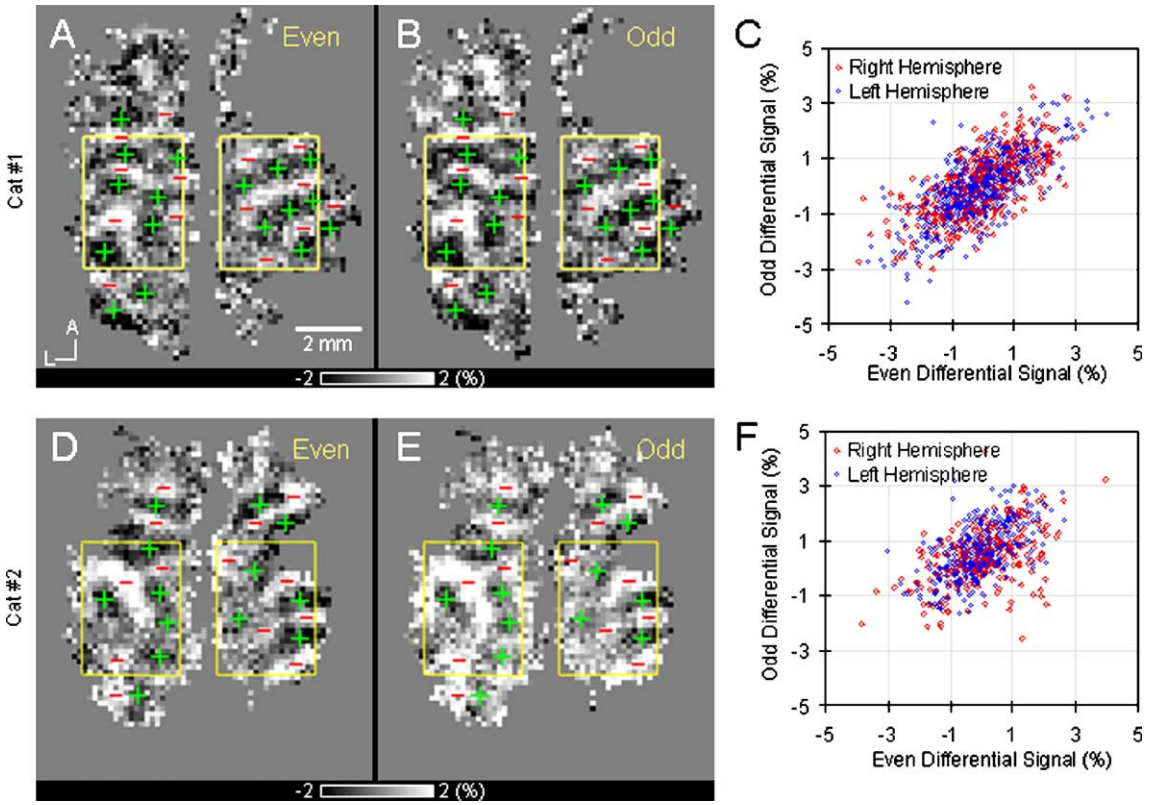

Fig. 4. Reproducibility of differential iso-orientation maps. CBV-weighted fMRI measurements for 0° orientation stimulus and the orthogonal 90° orientation stimulus were divided into two sub-groups, consisting of either even or odd runs. Each sub-group contains 20 runs in a study of one animal (A–C) and 35 runs in a study of another animal (D–F). A, anterior; L, lateral. From even and odd subsets, separate differential iso-orientation maps were determined, and their cross correlation value was obtained. From differential iso-orientation maps corresponding to even runs (A and D), clusters in response to 0° and 90° gratings are indicated by green '+' and red '−' signs, respectively. Then these signs were overlaid on the differential iso-orientation maps corresponding to odd runs (B and E). Signal changes within the yellow rectangular ROIs of the odd differential maps (B and E) were plotted against those of the corresponding even differential map (A and D) in C and F, respectively, where red and blue data points originate from the right and left hemispheres, respectively. Right side of images is the right hemisphere. The cross correlation value is 0.68 ($P = 4.5 \times 10^{-70}$) and 0.74 ($P = 4.2 \times 10^{-90}$) for right and left hemispheres in C and 0.51 ($P = 3.2 \times 10^{-22}$) and 0.59 ($P = 2.3 \times 10^{-33}$) for right and left hemispheres in F.

optical imaging signals originate from total hemoglobin. Also, the anatomical origins of optical imaging and MRI signals probably account for the dissimilarity in differential orientation responses. Intrinsic optical signals, measured at the cortical surface, are an integration of an unknown weighted sum of signals over upper cortical layers; these regions include non-specific surface vessels, whose signal may be removed by post-processing techniques such as principal component analysis (Sheth et al., 2004; Vanzetta et al., 2004). However, the CBV-weighted fMRI technique avoids acquisition of signal from surface vessels by selecting slices not

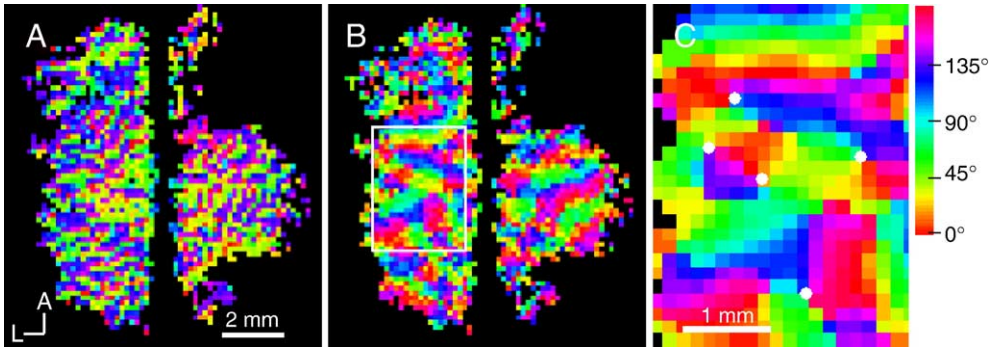

Fig. 5. Composite angle map for four stimulus orientations. In one animal, composite angle maps were created from data obtained with four different grating orientations (B). The color bar was used for color coding the resulting orientation preferences. As a control, a composite angle map was calculated from pre-stimulus baseline data (A). No spatial smoothing was applied in A and B. In the left hemisphere (marked by white rectangular box), changes between pixels preferentially activated by a particular stimulus orientation are smooth. For better visualization, signal changes in response to orientation stimulus were smoothed by a 3 × 3 Gaussian kernel, then a composite angle map was generated, with the region indicated by the white ROI in B expanded in C. "Pinwheel" structures indicated by small white dots were observed where domains for all orientations converge. A, anterior; L, left.

covering the surface of the cortex, thus improving the spatial specificity.

Our ratio of orientation-selective to non-orientation-selective responses (1.69) indicates the existence of non-orientation selective signal changes in both active and inactive columns. The non-orientation selective signals can be due to a contribution from sub-threshold synaptic activity in inactive domains (Das and Gilbert, 1995; Logothetis et al., 2001), a less-specific CBV response compared to metabolic and neural activity (Malonek and Grinvald, 1996), non-optimal visual stimuli for some populations of neurons (due to the use of only two orientations), non-ideal slice selection relative to the direction of columnar organization, and/or limited spatial resolution (pixels contain neurons with varying responses to orientation of stimuli).

Our data support the notion that both CBV and CBF regulate at a cortical columnar level (Duong et al., 2001). Since CBF is related to both CBV and blood velocity, it is expected that measurements of CBF and CBV responses induced by neural activity should be well correlated. The ratio of responses between preferred and orthogonal orientations indicates the selectivity of signals for detecting columnar structures; the CBV ratio of 1.69 in this study is poor compared to a previously measured CBF ratio of 3.30 (Duong et al., 2001). The difference in CBV and CBF ratios can be partly explained by the non-linear relationship between CBV and CBF: $CBV \propto CBF^{0.4}$ (Grubb et al., 1974; Lee et al., 2001).

Columnar resolution mapping capability of CBV and CBF-weighted fMRI techniques can be explained by the arrangement of arterial vascular structures. One intracortical artery supplies blood to a certain cortical volume (Woolsey et al., 1996). This cortical volume can be independently regulated by the dilation of intracortical arteries and small arterioles, with the possibility of finer control occurring within capillaries. As long as the volume supplied by each intracortical artery is smaller than the size of functional domains, functional structures should be resolvable by blood flow responses. Since space between intracortical arteries in cats is ~250 μm (Mchedlishvili and Kuridze, 1984), responses from columns separated by >500 μm should be individually distinguishable using CBV-weighted fMRI. In the human cerebral cortex, the number of penetrating arteries was found to be 4 times higher than that of emerging veins (Duvernoy et al., 1981). Thus, functional mapping methodologies based on arterial vascular responses should provide a higher spatial specificity than techniques based on venous vascular responses (such as BOLD).

Implication for columnar resolution fMRI in humans

These CBV-weighted high-resolution fMRI studies demonstrate that the CBV response is specific enough to cortical columns for columnar mapping in animals. Advantages of the contrast agent-induced CBV-weighted fMRI technique include a reduction of large vessel contributions, an increase in sensitivity, and a high specificity to parenchyma (Kim and Ugurbil, 2003; Mandeville and Marota, 1999). The disadvantage is a need for a relatively large dose (5–15 mg Fe/kg body weight) of long half-life contrast agents, which is not approved for use in human studies. Thus, the contrast agent-based CBV-weighted fMRI technique is currently limited to animal high-resolution fMRI research (Kim and Ugurbil, 2003).

Alternative fMRI approaches use blood as an endogenous tracer; these include conventional BOLD, early negative BOLD dip, and CBF-weighting techniques. The conventional gradient-echo BOLD technique has been mostly used for columnar mapping due to its high sensitivity and temporal resolution (Cheng et al., 2001; Dechent and Frahm, 2000; Goodyear and Menon, 2001; Menon and Goodyear, 1999; Menon et al., 1997). However, this approach is hampered by the contribution from large draining veins, which can dominate the stimulation-induced signal changes. To minimize the large vessel contributions and non-selective signals, a differential imaging approach has been employed (Cheng et al., 2001; Menon and Goodyear, 1999). However, if functional territories activated by different stimuli overlap, then 'common' active regions will also be removed in these differential functional maps, restricting application of this method to fMRI studies where stimulation conditions are known in advance to yield complementary responses. Alternatively or additionally, conventional BOLD data acquired before the draining effect is significant in pial vessels (e.g., less than 2 s) may be used for high-resolution studies (Goodyear and Menon, 2001). This requires high spatial and temporal resolution, and consequently has poor sensitivity when signal averaging time is limited. It has also been suggested that spin-echo BOLD techniques be used at high fields (Lee et al., 1999; Zhao et al., 2004). Although this approach is promising, it has a poor temporal resolution and increased RF power deposition in tissue, especially at high fields. A combination of the differential approach with these improved BOLD techniques is an excellent choice for mapping cortical columns where functional domains of orthogonal stimuli are complementary (such as for ocular dominance columns and orientation columns).

In order to obtain *single-condition* columnar maps, imaging signals must be specific to parenchyma or capillaries. Theoretically, the early dip indicative of local oxygen consumption changes (Thompson et al., 2003) should be the most specific to active neuronal sites. The initial dip should occur at capillaries near active neurons which drain first into venules, and eventually into large vessels including pial veins. Thus, the spatial localization of the dip changes dynamically, and the only first few seconds of data acquired after the onset of stimulation have high spatial specificity (Duong et al., 2000). It should be noted that the duration and magnitude of the dip in anesthetized cats are closely related to physiological conditions including anesthesia level, end-tidal CO_2, and blood pressure (Fukuda et al., 2004b; Harel et al., 2002; Kim and Duong, 2002). Consequently, the early dip is highly susceptible to physiological fluctuations as well as basal conditions and also has low overall sensitivity. Since sufficient signal averaging cannot be performed due to limited experimental time, the dip is not practically useful (Duong et al., 2000; Kim and Ogawa, 2002).

Lastly, the tissue-specific CBF response has successfully mapped submillimeter functional domains in anesthetized cats (Duong et al., 2001). The intrinsic specificity of hemodynamic signals is poor compared to that of tissue metabolic signals. But, among the available hemodynamic fMRI approaches, the CBF-based signal is expected to be the most specific to neural active sites because signals mostly originate from tissue and capillaries which are close to active neurons (Edelman et al., 1994; Kim, 1995; Kwong et al., 1992). As previously discussed, the ratio of CBF responses between preferred and orthogonal orientations is ~2 times higher than that of CBV response, indicating that the CBF response has intrinsically higher orientation selectivity than the CBV response. Even if the CBF technique has higher spatial specificity, its poor temporal resolution (e.g., 6 s for a CBF-

weighted image) results in a poorer sensitivity for a given imaging time. Further technical advances such as better imaging sequences, higher magnetic field strengths, and implementation of phase-array coils are essential to improve sensitivity of high-resolution CBF-weighted fMRI in humans. High-sensitivity CBV- or CBF-weighted MRI techniques without need for an exogenous contrast agent are desired for obtaining single-condition columnar maps.

Acknowledgments

Supported by NIH (EB002013, EB003375, EB003324, NS44589) and McKnight Foundation. The 9.4T MR system at the University of Pittsburgh was partly supported by NIH (RR17239). We thank Professor Kamil Ugurbil at the University of Minnesota for the use of a 9.4T MR system in our preliminary studies (supported by NIH RR08079), and Drs. Hiro Fukuda and Toshihiro Hayashi for insightful discussion and helpful suggestions.

References

Bonhoeffer, T., Grinvald, A., 1991. Iso-orientation domains in cat visual cortex are arranged in pinwheel-like pattern. Nature 353, 429–432.

Bonhoeffer, T., Grinvald, A., 1993. The layout of iso-orientation domains in area 18 of cat visual cortex: optical imaging reveals a pin-wheel-like organization. J. Neurosci. 13, 4157–4180.

Buxton, R.B., 2001. The elusive initial dip. Neuroimage 13, 953–958.

Cheng, K., Waggoner, R., Tanaka, K., 2001. Human ocular dominance columns as revealed by high-field functional magnetic resonance imaging. Neuron 32, 359–374.

Das, A., Gilbert, C.D., 1995. Long-range horizontal connections and their role in cortical reorganization revealed by optical recording of cat primary visual cortex. Nature 375, 780–784.

Dechent, P., Frahm, J., 2000. Direct mapping of ocular dominance columns in human primary visual cortex. NeuroReport 11, 3247–3249.

Duong, T.Q., Kim, D.-S., Ugurbil, K., Kim, S.-G., 2000. Spatio-temporal dynamics of the BOLD fMRI signals: toward mapping submillimeter columnar structures using the early negative response. Magn. Reson. Med. 44, 231–242.

Duong, T.Q., Kim, D.-S., Ugurbil, K., Kim, S.-G., 2001. Localized cerebral blood flow response at submillimeter columnar resolution. Proc. Natl. Acad. Sci. U. S. A. 98, 10904–10909.

Duvernoy, H., Delon, S., Vannson, J., 1981. Cortical blood vessels of the human brain. Brain Res. Bull. 7, 519–579.

Edelman, R.R., Siewert, B., Darby, D.G., Thangaraj, V., Nobre, A.C., Mesulam, M.M., Warach, S., 1994. Qualitative mapping of cerebral blood flow and functional localization with echo-planar MR imaging and signal targeting with alternating radio frequency. Radiology 192, 513–520.

Engel, A., Glover, G., Wendel, B., 1997. Retinotopic organization in human visual cortex and the spatial precision of functional MRI. Cereb. Cortex 7, 181–192.

Erinjeri, J.P., Woolsey, T.A., 2002. Spatial integration of vascular changes with neural activity in mouse cortex. J. Cereb. Blood Flow Metab. 22, 353–360.

Frostig, R.D., Lieke, E.E., Ts'o, D.Y., Grinvald, A., 1990. Cortical functional architecture and local coupling between neuronal activity and the microcirculation revealed by in vivo high-resolution optical imaging of intrinsic signals. Proc. Natl. Acad. Sci. U. S. A. 87, 6082–6086.

Fukuda, M., Rajagopalan, U.M., Homma, R., Matsumoto, M., Nishizaki, M., Tanifuji, M., in press. Localization of activity-dependent changes in blood volume to submillimeter-scale functional domains in cat visual cortex. Cereb. Cortex.

Fukuda, M., Wang, P., Kim, S.-G., 2004. Optical imaging of intrinsic signal and multi-unit activity in cat primary visual cortex during hypotension. Proc. 34th Annual Meeting of Society for Neuroscience. San Diego, p. 694.5.

Goodyear, B., Menon, R.S., 2001. Brief visual stimulation allows mapping of ocular dominance in visual cortex using fMRI. Hum. Brain Mapp. 14, 210–217.

Grinvald, A., Leike, E., Frostig, R.D., Gillbert, C.D., Wiesel, T.N., 1986. Functional architecture of cortex revealed by optical imaging of intrinsic signals. Nature 324, 361–364.

Grubb, R.L., Raichle, M.E., Eichling, J.O., Ter-Pogossian, M.M., 1974. The effects of changes in PaCO2 on cerebral blood volume, blood flow, and vascular mean transit time. Stroke 5, 630–639.

Harel, N., Lee, S.-P., Nagaoka, T., Kim, D.-S., Kim, S.-G., 2002. Origin of negative blood oxygenation level-dependent fMRI signals. J. Cereb. Blood Flow Metab. 22, 908–917.

Hubel, D., Wiesel, T., 1962. Receptive fields, binocular interactions and functional architecture in the cat's visual cortex. J. Physiol. (Lond.) 160, 106–154.

Hyde, J., Biswal, B., Jesmanowicz, A., 2001. High-resolution fMRI using multislice partial k-space GR-EPI with cubic voxels. Magn. Reson. Med. 46, 114–125.

Kennan, R.P., Scanley, B.E., Innis, R.B., Gore, J.C., 1998. Physiological basis for BOLD MR signal changes due to neuronal stimulation: separation of blood volume and magnetic susceptibility effects. Magn. Reson. Med. 40, 840–846.

Kim, S.-G., 1995. Quantification of relative cerebral blood flow change by flow-sensitive alternating inversion recovery (FAIR) technique: application to functional mapping. Magn. Reson. Med. 34, 293–301.

Kim, D.-S., Bonhoeffer, T., 1994. Reverse occlusion leads to a precise restoration of orientation preference maps in visual cortex. Nature 370, 370–372.

Kim, S.-G., Duong, T.Q., 2002. Mapping cortical columnar structures using fMRI. Physiol. Behav. 77, 641–644.

Kim, S.-G., Ogawa, S., 2002. Insights into new techniques for high resolution functional MRI. Curr. Opin. Neurobiol. 12, 607–615.

Kim, S.-G., Ugurbil, K., 2003. High-resolution functional magnetic resonance imaging of the animal brain. Methods 30, 28–41.

Kim, S.-G., Hu, X., Adriany, G., Ugurbil, K., 1996. Fast interleaved echo-planar imaging with navigator: high resolution anatomic and functional images at 4 Tesla. Magn. Reson. Med. 35, 895–902.

Kim, D.-S., Duong, T.Q., Kim, S.-G., 2000. High-resolution mapping of iso-orientation columns by fMRI. Nat. Neurosci. 3, 164–169.

Kwong, K.K., Belliveau, J.W., Chesler, D.A., Goldberg, I.E., Weisskoff, R.M., Poncelet, B.P., Kennedy, D.N., Hoppel, B.E., Cohen, M.S., Turner, R., et al., 1992. Dynamic magnetic resonance imaging of human brain activity during primary sensory stimulation. Proc. Natl. Acad. Sci. U. S. A. 89, 5675–5679.

Lee, S.-P., Silva, A.C., Ugurbil, K., Kim, S.-G., 1999. Diffusion-weighted spin-echo fMRI at 9.4 T: microvascular/tissue contribution to BOLD signal change. Magn. Reson. Med. 42, 919–928.

Lee, S.-P., Duong, T., Yang, G., Iadecola, C., Kim, S.-G., 2001. Relative changes of cerebral arterial and venous blood volumes during increased cerebral blood flow: implications for BOLD fMRI. Magn. Reson. Med. 45, 791–800.

Logothetis, N.K., 2000. Can current fMRI techniques reveal the micro-architecture of cortex? Nat. Neurosci. 3, 413.

Logothetis, N.K., Pauls, J., Augath, M., Trinath, T., Oeltermann, A., 2001. Neurophysiological investigation of the basis of the fMRI signal. Nature 412, 150–157.

Lowel, S., Freeman, B., Singer, W., 1987. Topographic organization of the orientation column system in large flat-mounts of the cat visual cortex: a 2-deoxyglucose study. J. Comp. Neurol. 255, 401–415.

Malonek, D., Grinvald, A., 1996. Interactions between electrical activity and cortical microcirculation revealed by imaging

spectroscopy: implication for functional brain mapping. Science 272, 551–554.
Mandeville, J.B., Marota, J.A., 1999. Vascular filters of functional MRI: spatial localization using BOLD and CBV contrast. Magn. Reson. Med. 42, 591–598.
Mandeville, J.B., Marota, J.J., Kosofsky, B.E., Keltner, J.R., Weissleder, R., Rosen, B.R., 1998. Dynamic functional imaging of relative cerebral blood volume during rat forepaw stimulation. Magn. Reson. Med. 39, 615–624.
Mchedlishvili, G., Kuridze, N., 1984. The modular organization of the pial arterial system in phylogeny. J. Cereb. Blood Flow. Metab. 4, 391–396.
Menon, R.S., Goodyear, B.G., 1999. Submillimeter functional localization in human striate cortex using BOLD contrast at 4 Tesla: implications for the vascular point-spread function. Magn. Reson. Med. 41, 230–235.
Menon, R.S., Ogawa, S., Strupp, J.P., Ugurbil, K., 1997. Ocular dominance in human V1 demonstrated by functional magnetic resonance imaging. J. Neurophysiol. 77, 2780–2787.
Ogawa, S., Lee, T.-M., Nayak, A.S., Glynn, P., 1990. Oxygenation-sensitive contrast in magnetic resonance image of rodent brain at high magnetic fields. Magn. Reson. Med. 14, 68–78.
Press, W.H., Teukolsky, S.A., Vetterling, W.T., Flannery, B.P., 1992. Statistical Description of Data. Numerical Recipes in C. Cambridge Univ. Press, Cambridge, pp. 503–506.
Rao, S.C., Toth, L.J., Sur, M., 1997. Optically imaged maps of orientation preference in primary visual cortex of cats and ferrets. J. Comp. Neurol. 387, 358–370.
Rojer, A.S., Schwartz, E.L., 1990. Cat and monkey cortical columnar patterns modeled by bandpass-filtered 2D white noise. Biol. Cybern. 62, 381–391.
Sheth, S.A., Nemoto, M., Guiou, M., Walker, M., Pouratian, N., Hageman, N., Toga, A.W., 2004. Columnar specificity of microvascular oxygenation and volume responses: implications for functional brain mapping. J. Neurosci. 24 (3), 634–641.
Shmuel, A., Grinvald, A., 1996. Functional organization for direction of motion and its relationship to orientation maps in cat area 18. J. Neurosci. 16, 6945–6964.
Strupp, J.P., 1996. Stimulate: a GUI based fMRI analysis software package. Neuroimage 3, S607.
Thompson, J.K., Peterson, M.R., Freeman, R.D., 2003. Single-neuron activity and tissue oxygenation in the cerebral cortex. Science 299, 1070–1072.
Toth, L.J., Rao, S.C., Kim, D.-S., Somers, D., Sur, M., 1996. Subthreshold facilitation and suppression in primary visual cortex revealed by intrinsic signal imaging. Proc. Natl. Acad. Sci. 93, 9869–9874.
van Bruggen, N., Busch, E., Palmer, J.T., Williams, S.-P., de Crespigny, A.J., 1998. High-resolution functional magnetic resonance imaging of the rat brain: mapping changes in cerebral blood volume using iron oxide contrast media. J. Cereb. Blood Flow Metab. 18, 1178–1183.
Vanzetta, I., Slovin, H., Omer, D.B., Grinvald, A., 2004. Columnar resolution of blood volume and oximetry functional maps in the behaving monkey. Neuron 42, 843–854.
Woolsey, T.A., Rovainen, C.M., Cox, S.B., Henegar, M.H., Liang, G.E., Liu, D., Moskalenko, Y.E., Sui, J., Wei, L., 1996. Neuronal units linked to microvascular modules in cerebral cortex: response elements for imaging the brain. Cereb. Cortex 6, 647–660.
Zhao, F., Wang, P., Kim, S.-G., 2004. Cortical depth-dependent gradient-echo and spin-echo BOLD fMRI at 9.4T. Magn. Reson. Med. 51, 518–524.